Broadband Electrostatic Waves near the Lower-hybrid Frequency in the Near-Sun Solar Wind Observed by the Parker Solar Probe

Jinsong Zhao, David M. Malaspina, Thierry Dudok de Wit, Viviane Pierrard, Yuriy Voitenko, Giovanni Lapenta, Stefaan Poedts, Stuart D. Bale, Justin C. Kasper, Davin Larson, et al.

The Astrophysical Journal Letters, 938:L21 (9pp), 2022 October 20 https://doi.org/10.3847/2041-8213/ac92e3

Broadband Electrostatic Waves near the Lower-hybrid Frequency in the Near-Sun Solar Wind Observed by the Parker Solar Probe

Jinsong Zhao[1,2], David M. Malaspina[3,4], T. Dudok de Wit[5], Viviane Pierrard[6,7], Yuriy Voitenko[6], Giovanni Lapenta[8], Stefaan Poedts[8,9], Stuart D. Bale[10,11], Justin C. Kasper[12,13], Davin Larson[11], Roberto Livi[11], and Phyllis Whittlesey[11]

[1] Key Laboratory of Planetary Sciences, Purple Mountain Observatory, Chinese Academy of Sciences, Nanjing 210023, People's Republic of China
js_zhao@pmo.ac.cn
[2] School of Astronomy and Space Science, University of Science and Technology of China, Hefei 230026, People's Republic of China
[3] Astrophysical and Planetary Sciences Department, University of Colorado, Boulder, CO, USA
[4] Laboratory for Atmospheric and Space Physics, University of Colorado, Boulder, CO, USA
[5] LPC2E, CNRS, CNES, University of Orléans, Orléans, France
[6] Solar-Terrestrial Centre of Excellence, Space Physics Division, Royal Belgian Institute for Space Aeronomy, 3 av. Circulaire, 1180, Brussels, Belgium
[7] Center for Space Radiations, ELIC, Université Catholique de Louvain, 1348 Louvain-La-Neuve, Belgium
[8] Department of Mathematics, KU Leuven, Celestijnenlaan 200B, B-3001 Leuven, Belgium
[9] Institute of Physics, University of Maria Curie-Skłodowska, Pl.M. Curie-Skłodowska 5, 20-031 Lublin, Poland
[10] Physics Department, University of California, Berkeley, CA 94720-7300, USA
[11] Space Sciences Laboratory, University of California, Berkeley, CA 94720-7450, USA
[12] BWX Technologies, Inc., Washington, DC 20001, USA
[13] Climate and Space Sciences and Engineering, University of Michigan, Ann Arbor, MI 48109, USA
Received 2022 May 22; revised 2022 September 13; accepted 2022 September 19; published 2022 October 18

Abstract

Using Parker Solar Probe observations, this Letter reports for the first time the existence of broadband electrostatic waves below the electron cyclotron frequency in the near-Sun solar wind and even in the extended solar corona. These waves have enhanced power spectral densities of the electric fields near the lower-hybrid frequency f_{LH}, and their peak frequencies can be below or exceed f_{LH}. The perturbed electric fields are distributed between about 0.1 and 50 mV m^{-1}. Accompanying broadband electrostatic waves, strong electrostatic solitary structures can arise, and their peak amplitudes approach nearly 500 mV m^{-1}. Due to the appearance of considerable electric field fluctuations perpendicular to the background magnetic field, the observed waves would propagate obliquely. Moreover, this Letter conjectures the wavenumber and frequency information for the candidate of the wave mode nature being the oblique slow mode wave, the ion Bernstein wave, or the oblique fast-magnetosonic whistler wave. One important consequence of the observed waves is that they may regulate the electron heat flux in the near-Sun solar wind and in the solar corona.

Unified Astronomy Thesaurus concepts: Solar wind (1534); Plasma physics (2089); Space plasmas (1544)

1. Introduction

Plasma waves are known to affect or, under some conditions, to control the dynamics of charged particles in the near-Sun solar wind and in the solar atmosphere (Verscharen et al. 2019). Hence, exploring observational evidence for the existence of plasma waves is crucial for understanding which wave–particle interaction takes part in the particle dynamics therein. Before the launch of the Parker Solar Probe (PSP), only remote instruments (e.g., radio instruments) could provide indirect observations of plasma waves in the solar wind below 0.3 au (e.g., Reid & Ratcliffe 2014). In situ measurements from PSP can directly detect various types of plasma waves in the near-Sun solar wind. The four common electromagnetic wave modes, i.e., radio waves with frequencies higher than the local electron plasma frequency f_{pe} (e.g., Pulupa et al. 2020), whistler waves with frequencies between the lower-hybrid frequency f_{LH} and the electron cyclotron frequency f_{ce} (e.g., Agapitov et al. 2020; Jagarlamudi et al. 2021; Cattell et al. 2021), and Alfvén ion cyclotron and fast-magnetosonic whistler waves with frequencies near the proton cyclotron frequency f_{cp} (e.g., Bowen et al. 2020; Verniero et al. 2020; Shi et al. 2021; Klein et al. 2021), were found by PSP observations. In addition to these electromagnetic mode waves, PSP has already identified many types of electrostatic waves, for example, electron Bernstein waves with frequencies near the fundamental and harmonic frequencies of f_{ce} (Malaspina et al. 2020, 2021; Shi et al. 2022), unprecedented electrostatic waves at about f_{ce} (named as Type B and Type C; Malaspina et al. 2021), electrostatic waves at about $0.7f_{ce}$ (Malaspina et al. 2020), multiband electrostatic waves below f_{ce} (Shi et al. 2022), and ion acoustic waves (Mozer et al. 2020b, 2021a, 2021b). Nearly all observed electrostatic waves exhibit the narrowband frequency feature, and the only exception is the ion acoustic mode wave. Mozer et al. (2020b) have shown that ion acoustic waves can have a broadband frequency distribution, extending continuously from a few hundred hertz (about one tenth of f_{ce}) to several kilohertz (about the ion plasma frequency f_{pp}). However, these previous findings did not report the existence of broadband electrostatic waves near f_{LH} in the near-Sun solar wind.

Using PSP observations, this Letter will exhibit observational evidence for another kind of broadband electrostatic wave, which has not yet been reported in the near-Sun solar wind. Different from ion acoustic waves with frequencies of

about $0.1f_{ce}$–f_{pp} (Mozer et al. 2020b), the observed broadband waves in this Letter are distributed in the frequency range of about 0.1–4.4f_{LH}. These waves can even arise below the Alfvén surface. This Letter is organized as follows. Section 2 introduces the data and shows an overview of our broadband electrostatic waves. Section 3 exhibits the wave features. The conjectures for the mode nature are presented in Section 4. Lastly, Section 5 contains the conclusions and discussions.

2. Data and Overview

This Letter uses data from the FIELDS instrument (Bale et al. 2016) and Solar Wind Electrons Alphas and Protons (SWEAP) instrument (Kasper et al. 2016).

Electric field data from PSP come from five voltage sensors (V_1−V_5; Malaspina et al. 2016; Bale et al. 2016), in which V_1−V_4 are located in the plane of the PSP heat shield, and V_5 is mounted on the magnetometer boom. Using voltages measured by V_1−V_5, three differential voltages are defined as $dV_{12} = V_1 - V_2$, $dV_{34} = V_3 - V_4$, and $dV_z = V_5 - (V_1 + V_2 + V_3 + V_4)/4$. Through the Digital Fields Board in the instrument suite on PSP (Malaspina et al. 2016), these voltages and differential voltages are used to produce DC- and AC-coupled signals. We will use the DC-coupled power spectra to show the existence of broadband electrostatic waves. We will also use the electric field data (in units of V m^{-1}) through $E = -dV/L$ where $L = 3.5$ m corresponds to the antenna half-geometric length (Mozer et al. 2020a). The choice of $L = 3.5$ m is due to the waves studied in this Letter having the frequency roughly larger than 20 Hz, and this would underestimate E for the low–frequency (smaller than 20 Hz) waves (Mozer et al. 2020a). The magnetic field data we used come from the fluxgate magnetometer (MAG) and search coil magnetometer (SCM). Note that the three magnetic field components (B_u, B_v, B_w) measured by the SCM are given in the SCM sensor frame, and we also use MAG and electric field data in spacecraft coordinates (MAG sensor frame; Dudok de Wit et al. 2022), where the three axes are defined as x, y, and z, to analyze the wave feature. The relation between the SCM sensor frame and the MAG sensor frame was introduced by Bowen et al. (2020) and Dudok de Wit et al. (2022).

In order to show the waveform of the observed waves, electromagnetic field data with a high cadence are needed. Thus, we choose the data collected from 2021 April 27 to 2021 April 30 in Encounter 8, when the sample rates of FIELDS voltage sensors and the SCM are about 2340 samples/s for most of the time. For the plasma environment, we use Solar Probe Analyzer—Ions (SPAN-I; Livi et al. 2021) to give the solar wind speed, density, and temperature, and we use Solar Probe Analyzer—Electrons (SPAN-E; Whittlesey et al. 2020) to exhibit the electron information.

Figure 1 presents an overview of broadband electrostatic waves near f_{LH} between 00:00:00 UT on 2021 April 27 and 24:00:00 UT on 2021 April 30, when PSP reached perihelion ($15.9R_S$) at nearly 08:48 on 2021 April 29. Because $f_{pe} \gg f_{ce}$ during this time interval, $f_{LH} \simeq \sqrt{f_{cp} f_{ce}}$. We note that Kasper et al. (2021) have explored the fact that PSP crossed the extended corona below the Alfvén surface three times, i.e., 09:33–14:42 on 2021 April 28, 07:18–07:52 on 2021 April 29, and from 23:40 on 2021 April 29 to 01:24 on 2021 April 30.

Figure 1(a) presents the DC-coupled spectra $P_{dV_{12}}(f, t)$ of the potential difference dV_{12} between two voltage sensors V_1 and V_2, and Figure 1(b) further illustrates the distribution of $P_{dV_{12}}(f, t)$ normalized by its maximum $P^{max}_{dV_{12}}(t)$ in the frequency space at each time t. These two figures evidently show that $P_{dV_{12}}(f, t)$ is enhanced between several tens of hertz and several hundred hertz during about 02:00–24:00 UT on 2021 April 27 (labeled Interval I), and $P_{dV_{12}}(f, t)$ is also enhanced between several tens of hertz and about 1 kHz in the time interval from nearly 14:00 UT on 2021 April 28 to 24:00 on 2021 April 29 (labeled Interval II). We note that the enhancements in $P_{dV_{12}}(f, t)$ in the two subintervals (02:00–17:30 UT and 17:30–24:00 UT) in Interval I exhibit different frequency distribution features, that is, the wave frequencies are normally below f_{LH} during 02:00–17:30 UT and they are around f_{LH} during 17:30–24:00 UT. Figures 1(a) and (b) also exhibit signatures of narrowband waves higher than about 600 Hz near the heliospheric current sheets (HCSs) on 2021 April 29. Moreover, narrowband waves with different frequencies (about 300 Hz and several kilohertz) arise on 2021 April 30, and these waves are similar to ion acoustic waves reported by Mozer et al. (2021b) and multiband electrostatic waves reported by Shi et al. (2022).

Figure 1(c) presents the DC-coupled spectra $P_{B_v}(f, t)$ of the magnetic field component B_v. The spectra $P_{B_w}(f, t)$ are nearly the same as the $P_{B_v}(f, t)$ distribution (not shown). We note that due to an unknown anomaly in the data of B_u, the spectra of B_u are unreliable during our time interval of interest (Dudok de Wit et al. 2022). Figure 1(c) shows that $P_{B_v}(f, t)$ normally decreases with f. These spectra are not enhanced in the frequency band in which the enhancements of the electric field spectra arise.

The electromagnetic signatures shown in Figures 1(a)–(c) strongly support the existence of broadband electrostatic waves near f_{LH}. Therefore, we concentrate on patches of these wave activities in this study.

Furthermore, Figures 1(d)–(i) exhibit the magnetic field and plasma environment for the observed electrostatic waves near f_{LH}. The difference between the two environments in Intervals I and II is quite evident. In Interval I, the solar wind is relatively steady, and the averaged plasma parameters are $n_0 \simeq 308$ cm^{-3}, $V_0 \simeq 390$ km s^{-1}, $T_0 \simeq 69$ eV, and $B_0 \simeq 176$ nT. In Interval II, PSP crosses multiple HCSs, and the averaged plasma parameters are $n_0 \simeq 3756$ cm^{-3}, $V_0 \simeq 204$ km s^{-1}, $T_0 \simeq 32$ eV, and $B_0 \simeq 303$ nT. In addition, from the pitch angle distribution of electrons in the energy channel with 314 eV, we see that the pitch angle is about 180° in Interval I, which indicates the existence of a steady open magnetic field, and multiple transitions of the dominant direction of the pitch angle in Interval II, which result from multiple crossings of the HCS. These observations show that the observed electrostatic waves can occur in obviously different plasma environments. Moreover, from Figures 2 and 3, the waves in Interval I normally have a smaller amplitude than those in Interval II.

3. Events and Statistical Features

To illustrate basic observational features of broadband electrostatic waves, Figure 2 presents the distributions of the electric field and its power spectral density (PSD) for four wave events (named Events #1−#4). Events #1 and #2, respectively, represent the typical event in the two subintervals 02:00–17:30 UT and 17:30–24:00 UT in Interval I. Event #3 illustrates the waves with two frequency peaks, and Event #4 illustrates the existence of solitary structures with considerably large electric fields. Both Events #3 and #4 come from Interval II.

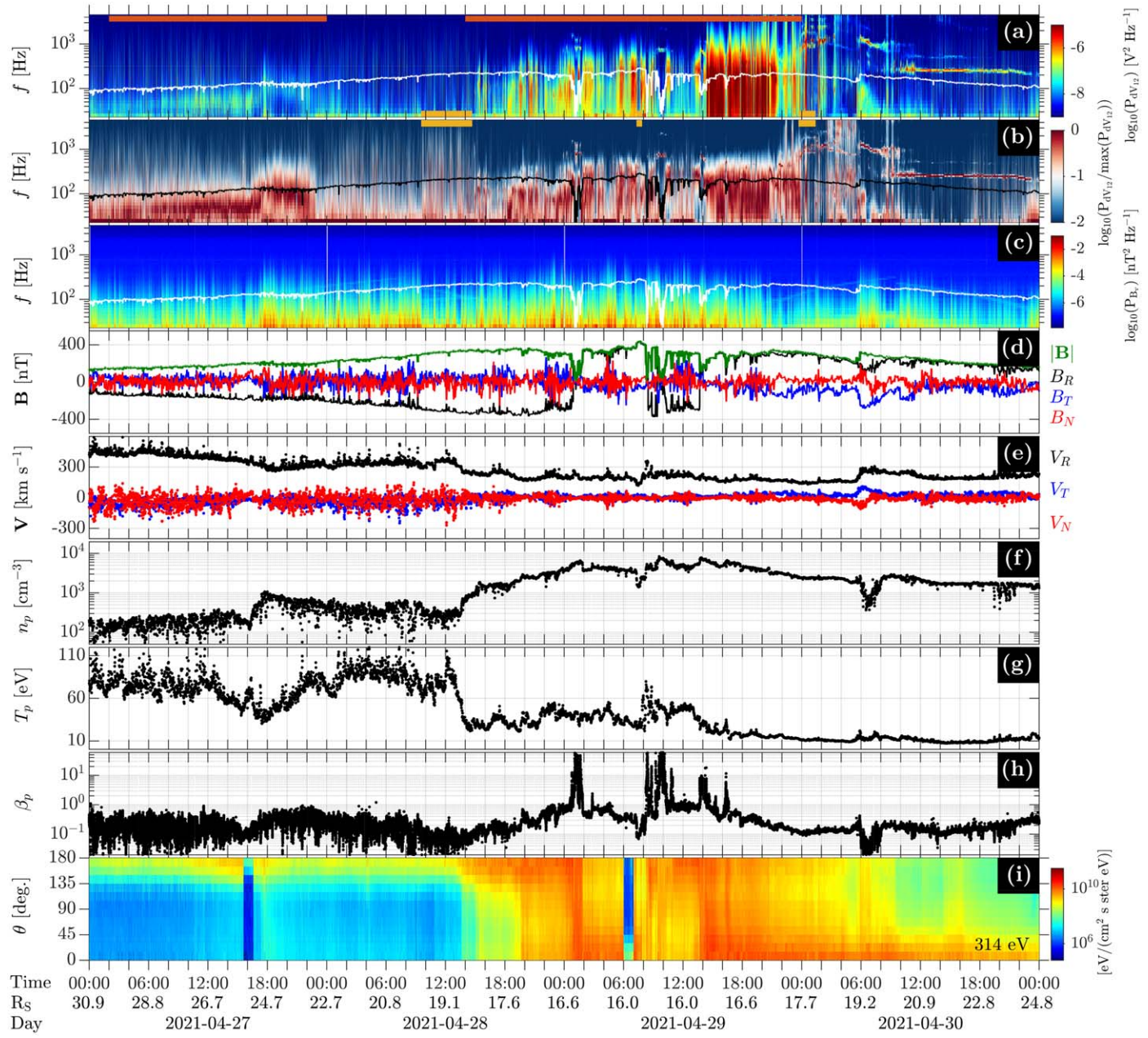

Figure 1. Overview of broadband electrostatic waves and the plasma environment. (a) DC-coupled spectra of the potential difference dV_{12} between V_1 and V_2, $P_{dV_{12}}$; (b) the normalized DC-coupled spectra $P_{dV_{12}}/P_{dV_{12}}^{\max}$, where $P_{dV_{12}}^{\max}$ denotes the maximum $P_{dV_{12}}$ at each time; (c) DC-coupled spectra of the magnetic field component B_v, P_{B_v}; (d) the magnetic field $\boldsymbol{B}$ in radial–tangential–normal (RTN) coordinates and magnetic field strength $|\boldsymbol{B}|$; (e) the solar wind speed $\boldsymbol{V}$ in RTN coordinates; (f) the proton number density, n_p; (g) the proton temperature, T_p; (h) the plasma beta β_p defined as the ratio between the proton thermal pressure and the magnetic pressure; and (i) the pitch angle distribution of electrons in the energy channel with $E_e \simeq 314$ eV. The orange bars in the top of panel (a) label the two time intervals: 02:00:00–24:00:00 UT on 2021 April 27 (Interval I) and from 14:00:00 UT on 2021 April 28 to 24:00:00 UT on 2021 April 29 (Interval II). The yellow bars in the bottom of panel (a) and in the top of panel (b) highlight that PSP entered the extended corona below the Alfvén surface during the time intervals 09:33–14:42 on 2021 April 28, 07:18–07:52 on 2021 April 29, and from 23:40 UT on 2021 April 29 to 01:24 on 2021 April 30. The lower-hybrid frequency is denoted by the white curves in panels (a) and (c) and by the black curve in panel (b).

In Event #1 shown in Figure 2(a), electrostatic waves are located in the frequency band $f_{\rm band} \sim 20$–200 Hz, where the peak frequency is $f_{\rm peak} \simeq 50$ Hz $\sim 0.5 f_{\rm LH}$. The peaks in $|\boldsymbol{E}_{\rm fil}|$ are of the order of 1 mV m^{-1}.

In Event #2 shown in Figure 2(b), for electrostatic waves with $f \simeq 50$–200 Hz, the peak frequency is nearly equal to $f_{\rm LH}$, i.e., $f_{\rm peak} \simeq 130$ Hz $\sim 1.1 f_{\rm LH}$, and the wave amplitude seems slightly larger than that in Event #1.

Event #3 resides near an HCS that occurred at 00:54:50 UT on 2021 April 29. Broadband electrostatic waves in Event #3 have $f_{\rm band} \sim 30$–400 Hz, as shown in Figure 2(c). These waves have two peak frequencies, $f_{\rm peak} \simeq 0.5 f_{\rm LH}$ and $1.3 f_{\rm LH}$, and the strong peaks in $|\boldsymbol{E}_{\rm fil}|$ are about $\sim$30 mV m^{-1}.

Event #4 contains extremely strong electric field structures, as shown in Figure 2(d). The magnitude of the electric field can reach 500 mV m^{-1}. These structures behave as dipole electric field structures (a dip followed by a peak in E_x and a peak followed by a dip in E_y, see panel (d-VI)), and these electric field structures are similar to electric field behaviors of electrostatic solitary structures (e.g., Malaspina et al. 2013;

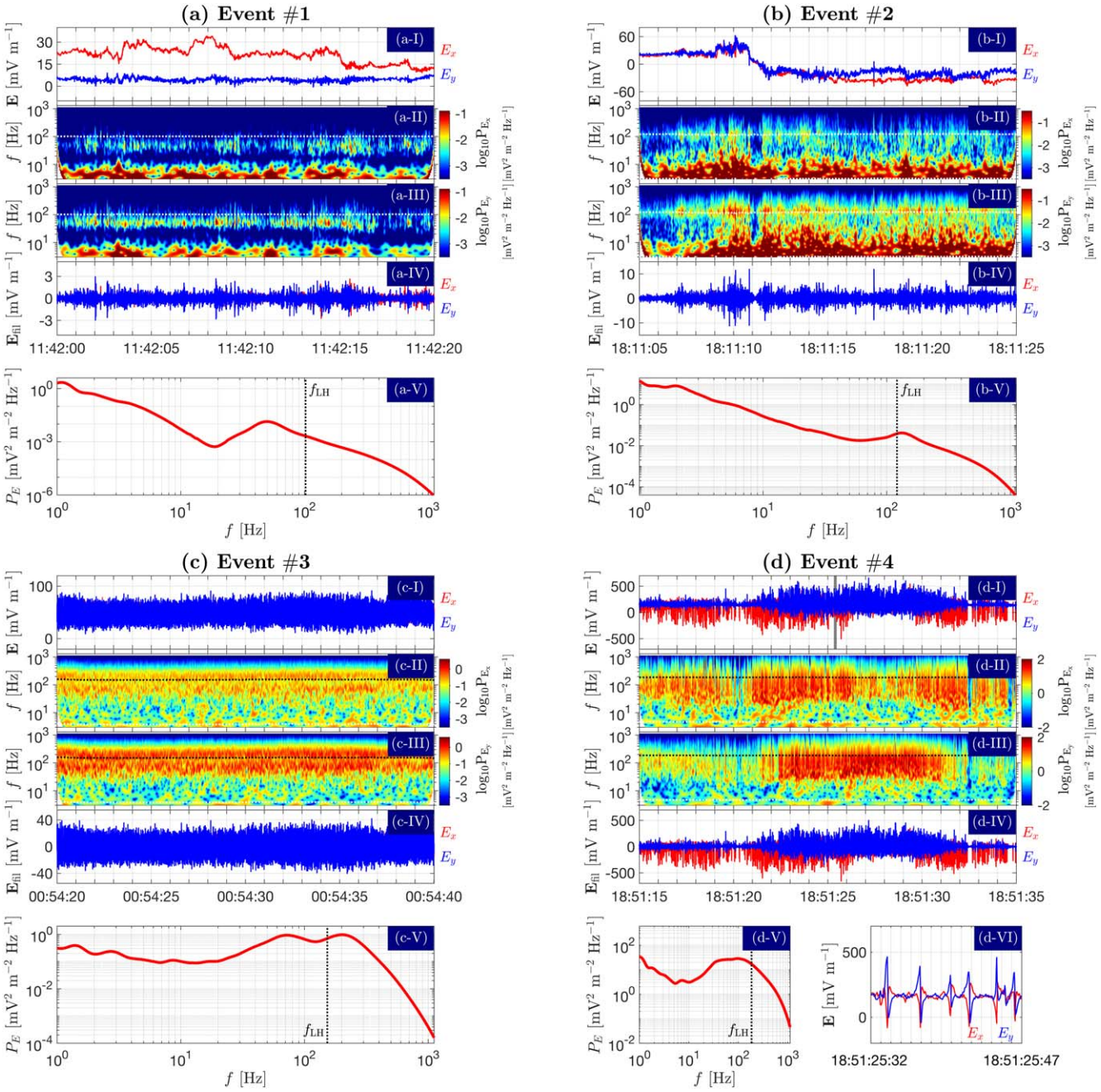

Figure 2. The electric field and its power spectral density in four different events: (a) Event #1; (b) Event #2; (c) Event #3; and (d) Event #4. Panel (I) shows two-dimensional electric fields $\boldsymbol{E}$ in the spacecraft frame, panel (II) shows the spectrogram of E_x, panel (III) shows the spectrogram of E_y, panel (IV) shows the filtered electric field $\boldsymbol{E}_{\rm fil}$, and panel (V) shows the mean PSD of $\boldsymbol{E}$. Panel (d-VI) zooms in $\boldsymbol{E}$ in the time interval 18:51:25:32–47 UT (shaded gray in panel (d-I)). The dotted lines in spectrograms of $\boldsymbol{E}$ denote the lower-hybrid frequency.

Graham et al. 2021; Mozer et al. 2021a). The relation between these electrostatic solitary structures and broadband electrostatic waves near $f_{\rm LH}$ will be investigated in future work.

Based on the observed features of the four events, we select wave events by identifying the local enhancement of $W_E \equiv |\delta\boldsymbol{E}(f)|^2 = \delta E_x^2(f) + \delta E_y^2(f)$ between $f_{\rm cp}$ and $f_{\rm ce}$. An automated identification method is developed to exhibit the statistical distributions of broadband electrostatic waves through the following procedures.

1. We use the Morlet wavelet decomposition to give $\delta\boldsymbol{E}(f, t)$ in the time interval $\Delta t = 3.5$ s (the same as the SPAN-I cadence). Then, the median value of $\delta\boldsymbol{E}(f, t)$ at each f, that is $\delta\boldsymbol{E}(f)$, is picked up to proceed to the next procedure.
2. Based on W_E at $f > 0.1f_{\rm LH}$, we look for the strongest peak ($W_{E\rm peak}$) through the maximum W_E and discriminate its two edges ($f_{\rm lower}$ and $f_{\rm upper}$) under the condition $W_E = 0.05W_{E\rm peak}$. This threshold value is given by experience. We record these values when $f_{\rm lower} < f_{\rm LH}/2$.
3. We filter $\boldsymbol{E}_{\rm sc}$ in the frequency band $[f_{\rm lower}, f_{\rm upper}]$, and thus we can estimate the wave amplitudes in different conditions based on the filtered electric fields $\delta E_{{\rm fil}x}$ and $\delta E_{{\rm fil}y}$. We record the median value of peaks of the absolute values of $\delta E_{{\rm fil}x}$ and $\delta E_{{\rm fil}y}$ to give the wave amplitude δE. We also record the median value of the top 20% of these peaks to describe the strong electric field fluctuation part during Δt, and this value is denoted as δE_s. Moreover, in

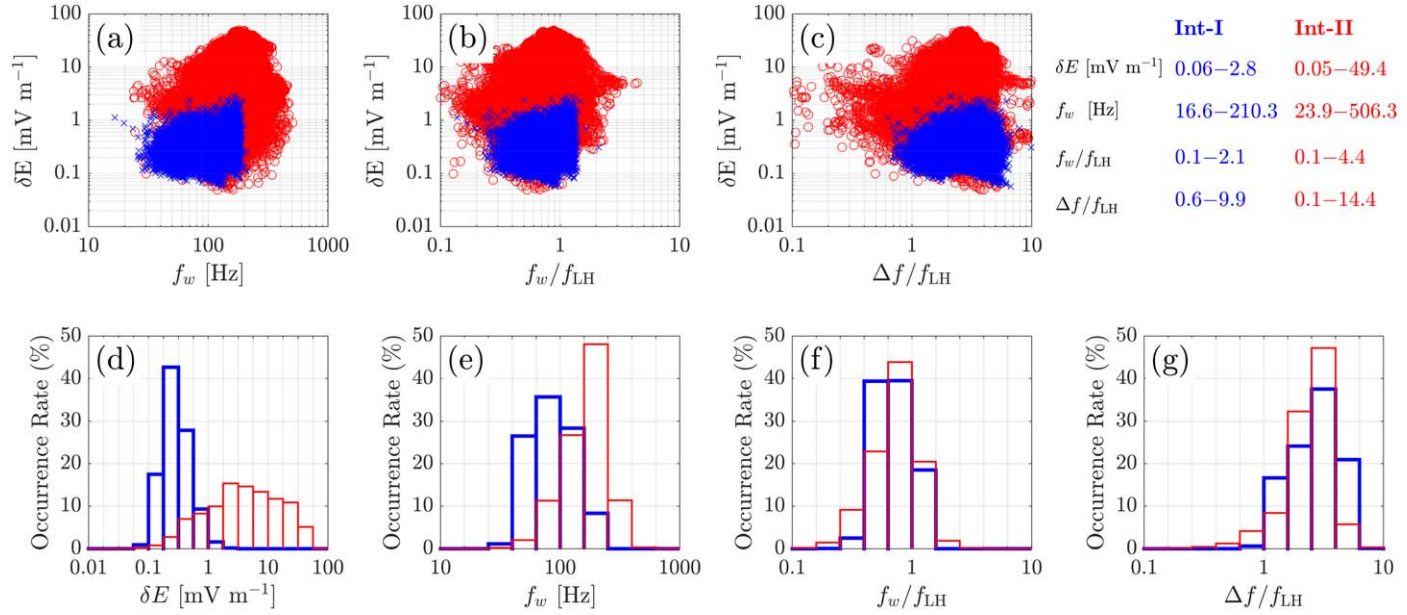

Figure 3. Statistical results of primary wave parameters. (a) The joint distribution of the wave amplitude δE and the weighted wave frequency f_w, (b) the joint distribution of δE and the normalized wave frequency f_w/f_{LH}, and (c) the joint distribution of δE and the normalized wave frequency band $\Delta f/f_{LH}$, where the crosses and circles highlight data belonging to Intervals I and II, respectively. Histograms of (d) δE, (e) f_w, (f) f_w/f_{LH}, and (g) $\Delta f/f_{LH}$, where the blue and red curves denote the wave data sets in Intervals I and II, respectively.

order to exclude narrowband electrostatic waves at about 600 Hz, we record δE_{high} for the high-frequency waves in the frequency range [600 Hz, f_{upper}] when $f_{upper} > 600$ Hz, and then we collect the events with $\delta E > 3\delta E_{high}$. We note that these narrowband electrostatic waves are not analyzed in this Letter.

Finally, the plasma parameters for each wave event are directly obtained from SPAN-I data.

Following these identification procedures, we collect 45,073 events for broadband electrostatic waves in the time interval from 00:00:00 UT on 2021 April 27 to 24:00:00 UT on 2021 April 29. The total duration is about 44 hr.

Figure 3 exhibits the statistical results of primary wave parameters.

Figure 3(a) presents the joint distribution of δE and the weighted wave frequency defined as $f_w \equiv \sum_{f_{lower}}^{f_{upper}} f W_E(f) \Big/ \sum_{f_{lower}}^{f_{upper}} W_E(f)$. From this figure, we see that f_w is distributed around 16.6–210.3 Hz in Interval I and around 23.9–506.3 Hz in Interval II. Moreover, δE is distributed around 0.1–2.8 mV m^{-1} in Interval I and around 0.1–49.4 mV m^{-1} in Interval II. We note that for the strong electric field fluctuation part, δE_s is distributed around 0.2–17.3 mV m^{-1} in Interval I and around 0.2–258.0 mV m^{-1} in Interval II (not shown).

Figures 3(b) and (c) present the dependence of δE on the normalized frequency f_w/f_{LH} and on the normalized frequency band $\Delta f/f_{LH}$, respectively. These two figures show that $f_w/f_{LH} \sim 0.1$–2.1 and $\Delta f/f_{LH} \sim 0.6$–9.9 in Interval I, and $f_w/f_{LH} \sim 0.1$–4.4 and $\Delta f/f_{LH} \sim 0.1$–14.4 in Interval II.

Figures 3(d)–(g) further present the occurrence rate of the observed waves as a function of δE, f_w, f_w/f_{LH}, and $\Delta f/f_{LH}$, respectively. An interesting result is that although the dependence of the occurrence rate on δE (f_w) in Intervals I and II seems obviously distinct, the occurrence rate distributions of f_w/f_{LH} and $\Delta f/f_{LH}$ in Intervals I and II exhibit roughly the same tendency. The majority of the observed waves are concentrated in $f_w/f_{LH} \sim 0.3$–2 and $\Delta f/f_{LH} \sim 1$–6.

Figure 4 presents the statistical distributions of primary plasma parameters.

Figure 4(a) shows the joint distribution of n_p and β_p to separate the wave events in Interval I from those in Interval II. This figure shows that β_p is often smaller than 1 in Interval I, whereas β_p can extend to about 10 in Interval II. Figure 4(b) further shows the occurrence rate of the observed waves as a function of β_p, and we see that the majority of the wave events are distributed in $\beta_p \sim 0.03$–0.6 in Interval I and in $\beta_p \sim 0.06$–3 in Interval II.

Figure 4(c) shows the occurrence rate of the observed waves as a function of θ_{BR} (the angle between the magnetic field $\boldsymbol{B}$ and radial direction $\boldsymbol{R}$). The wave events are concentrated around $\theta_{BR} \sim 0°$ and around 180°. Because data for all time exhibit a similar distribution, broadband electrostatic waves seem to occur no matter whether the magnetic field is radial or not.

Figure 4(d) shows the occurrence rate of the observed waves as a function of θ_{BV} (the angle between $\boldsymbol{B}$ and the solar wind velocity $\boldsymbol{V}$). Because $\boldsymbol{V}$ is slightly deviating from the radial direction, the wave data and all data are both concentrated in the bins $\theta_{BV} = 15°$–30° and 150°–165°. This figure shows that broadband electrostatic waves occur at arbitrary θ_{BV}.

4. The Mode Nature

According to the electromagnetic features (evident signature in the electric field fluctuations but not in the magnetic field fluctuations) and the wave frequency below f_{ce} for the observed waves, the possible candidates for the mode nature are: (I) the parallel ion acoustic wave; (II) the oblique slow mode (or oblique ion acoustic) wave; (III) the ion Bernstein wave; and (IV) the oblique fast-magnetosonic whistler wave. We note that when the fast-magnetosonic whistler wave propagates nearly

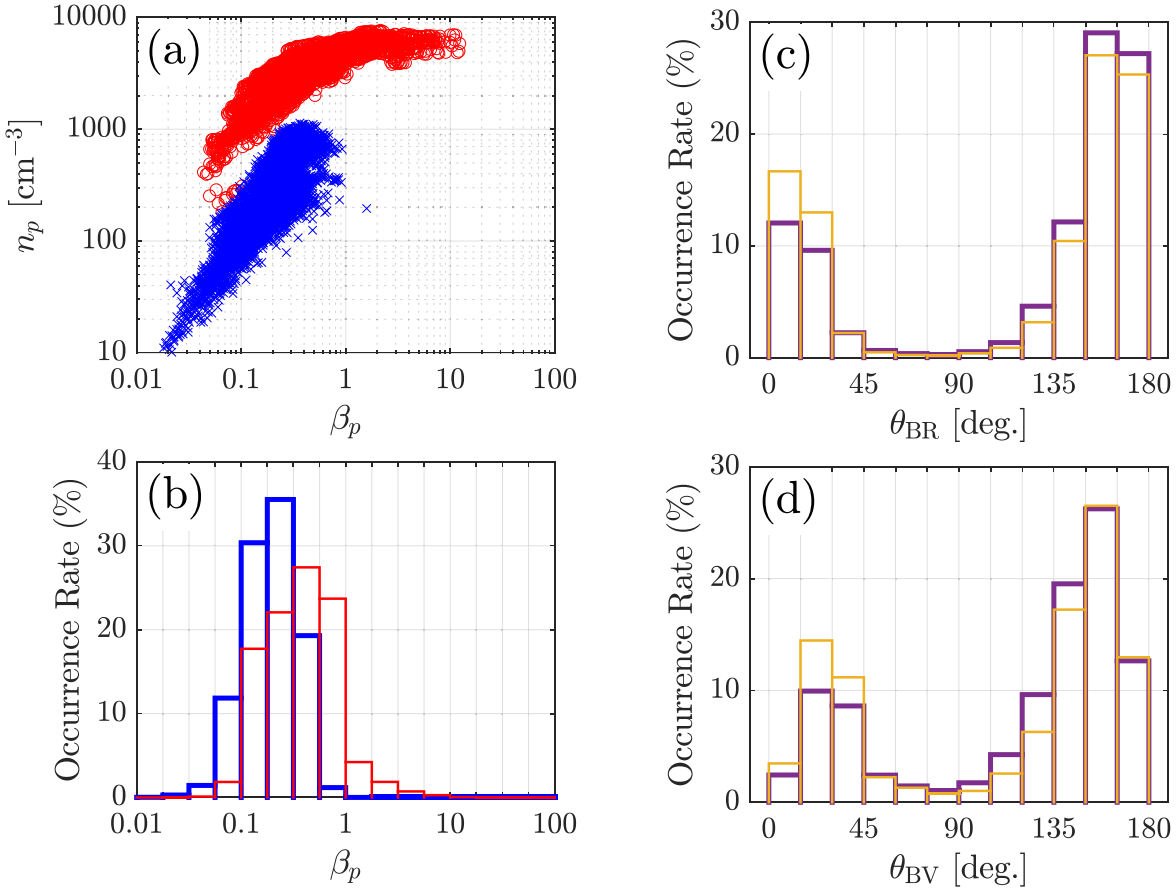

Figure 4. Dependence of statistical results on primary plasma parameters. (a) The joint distribution of n_p and β_p, and (b) histogram of β_p, where the wave data sets in Intervals I and II are denoted by blue and red, respectively. (c) Histograms of θ_{BR} (the angle between the magnetic field $\boldsymbol{B}$ and the radial vector $\boldsymbol{R}$), and (d) histograms of θ_{BV} (the angle between the magnetic field $\boldsymbol{B}$ and the radial vector $\boldsymbol{V}$), where the orange and purple curves denote the data of wave events and data for all time, respectively.

perpendicular to the magnetic field, this wave is particularly named the lower-hybrid wave.

Because the parallel ion acoustic wave (Candidate I) is a pure electrostatic mode wave, that is, $\boldsymbol{k}\cdot\delta\boldsymbol{E}\neq 0$ and $\boldsymbol{k}\times\delta\boldsymbol{E}=0$, its electric field perturbation is along the magnetic field (Mozer et al. 2020b), i.e., $\delta E_{\parallel}\neq 0$ and $\delta E_{\perp}=0$. In order to test this prediction from observations, a joint distribution between δE and B_z/B_0 is presented in Figure 5(a). Because PSP only measures the two-dimensional field $\boldsymbol{E}=\boldsymbol{E}_x+\boldsymbol{E}_y$ inthe spacecraft frame, $\delta E=\sqrt{\delta E_x^2+\delta E_y^2}$ at large B_z/B_0 (i.e., $B_z/B_0\rightarrow 1$) approximates $\delta E_{\perp}$. Figure 5(a) shows large numbers of wave events (33,310 out of a total of 45,073 events) existing at $B_z>0.9B_0$. This indicates that these waves cannot be parallel ion acoustic waves. One may be interested in the problem of how unknown δE_z affects our conclusion. When we consider $\delta E_z\sim\delta E_x\sim\delta E_y$, the perpendicular part of δE_z, i.e., $\delta E_z\times\sin(\theta_{B_zB_0})<0.01\delta E_z$, is much smaller than $\delta E_x\sim\delta E_y$ at $B_z>0.9B_0$, and this cannot considerably change the values of $\delta E_{\perp}$ therein. Here, $\theta_{B_zB_0}$ denotes the angle between B_z and B_0.

Unfortunately, PSP did not provide high-resolution measurements of particles and three-dimensional electric fields, and consequently we cannot perform direct observational identification among the candidates beyond Candidate I. Here, from the distributions of the wave frequency (shown in Figures 5(b) and (c)) and the theoretical predictions of plasma waves, we will propose possible wave parameters for Candidate II, III, or IV.

It is well known that the observed frequency $\omega_{sc}=2\pi f_{sc}$ consists of the frequency in the plasma frame $\omega_{pl}=2\pi f_{pl}$ and the Doppler shift frequency $\boldsymbol{V}\cdot\boldsymbol{k}$,

$$\omega_{sc}=\omega_{pl}+\boldsymbol{V}\cdot\boldsymbol{k}. \quad (1)$$

The competition between ω_{pl} and $\boldsymbol{V}\cdot\boldsymbol{k}$ is determined by the relation between the wave phase velocity $v_p=\omega_{pl}/k$ and the solar wind speed along the wavevector $V_k\equiv\boldsymbol{V}\cdot\boldsymbol{k}/k$. Thus, in order to know v_p of each candidate for evaluating this competition, we consider basic features of these three mode waves at typical wave-normal angles $\theta=75^{\circ}$ and $89^{\circ}.9$ in the two-component (proton and electron) plasma model, as shown in Figure 5. The magnetic field and proton parameters correspond to the average values in Interval I, and the number density and temperature of the electron population are assumed as $n_e=n_p$ and $T_e=3T_p$. This choice of T_e is based on the statistical relation between the temperatures of core electrons and protons at $V\sim 300$ km s^{-1} (average solar wind speed in Interval I) found by Halekas et al. (2020). We note that this T_e assumption merely provides an approximate description for the waves in actual varying plasma environments.

According to previous theoretical studies of the kinetic slow mode wave (e.g., Zhao et al. 2014; Narita & Marsch 2015; Verscharen et al. 2017), its phase speed is approximately $v_p=C_Sk_{\parallel}/k$, where C_S denote the ion acoustic speed and $k_{\parallel}$ is the wavenumber parallel to the magnetic field. The

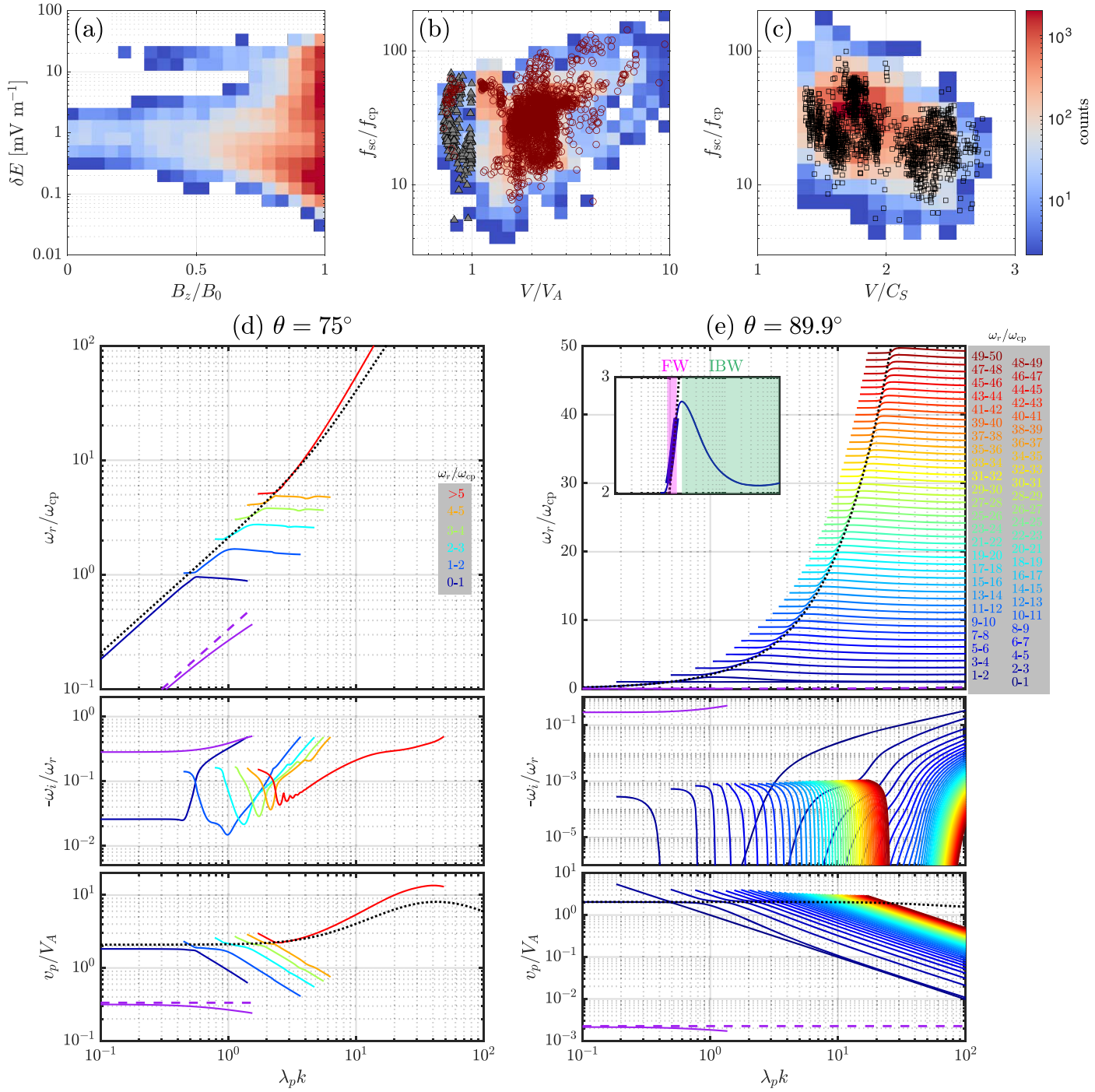

Figure 5. Analyses of the wave nature. (a) The joint distribution of B_z/B_0 and δE. (b) The joint distribution of V/V_A and f_{sc}/f_{cp}, where the solid triangles denote the data with $V/V_A < 1$ and circles denote the events with $\theta_{BV} = 42.^{\circ}5$–$47.^{\circ}5$. (c) The joint distribution between V/C_S and f_{sc}/f_{cp}, where the squares denote the events with $\theta_{BV} = 0°$–$10°$. Real frequencies ω_r (normalized by $\omega_{cp} = 2\pi f_{cp}$), damping rates ω_i (normalized by ω_r), and phase speeds $v_p = \omega_r/k$ of the fast-magnetosonic whistler waves (FW) and ion Bernstein wave (IBW) at two wave-normal angles: (d) $\theta = 75°$; and (e) $\theta = 89.^{\circ}9$. Oblique slow mode waves are also overlaid in panels (d) and (e), where the purple solid curves correspond to the numerical solution of the complete dispersion equation in the linear kinetic theory, and the purple dashed curves come from the analytical prediction $\omega_r = C_S k_\parallel$ (Verscharen et al. 2017). The black dotted curves denote the highly oblique fast-magnetosonic whistler wave predicted by the two-fluid model (Zhao 2015). The inset in panel (e) shows two parts of the wave between $2\omega_{cp}$ and $3\omega_{cp}$: the FW part ($v_g > V_A$, v_g denoting the group velocity) and the IBW part with $v_g < 0$. Note that the data with $|\omega_i| > \omega_r/2$ are discarded in panels (d) and (e), and only the harmonic waves below $50 f_{cp}$ are shown in panel (e).

plasma gyrokinetic theory predicts $C_S = \sqrt{k_B(3T_p + T_e)/m_p}$ (Verscharen et al. 2017), where k_B denotes the Boltzmann constant. The comparisons of the oblique slow mode wave between gyrokinetic and full kinetic models are shown in Figures 5(d) and (e). We see that $v_p = C_S k_\parallel/k$ can roughly describe the phase speed of the waves with $|\omega_i| < \omega_r/2$.

Ion Bernstein waves are located between the frequency band of $n\omega_{cp}$ and $(n+1)\omega_{cp}$ (n denotes a positive integer, and an example of the wave between $2\omega_{cp}$ and $3\omega_{cp}$ is shown in the inset in Figure 5(e); also see López et al. 2017), and their phase speeds can decrease from about $2V_A$ to a value much smaller than V_A with increasing wavenumber.

The oblique fast-magnetosonic whistler wave above $\omega_r > \omega_{cp}$ corresponds to many separated branches between the frequency band of $n\omega_{cp}$ and $(n+1)\omega_{cp}$ (López et al. 2017; Sun et al. 2021), and an example of the branch between $2\omega_{cp}$ and $3\omega_{cp}$ is shown in the inset in Figure 5(e). Figures 5(d) and (e) also exhibit the near-perpendicular fast-magnetosonic whistler wave predicted by the two-fluid model (Zhao 2015), i.e.,

$$\omega_r = V_A k[1 + \lambda_e^2 k^2 + \lambda_p^2 k_\parallel^2 + (1 + \lambda_e^2 k^2)^2(\beta_p + \beta_e) + k_\parallel^2/k_\perp^2]^{1/2}/(1 + \lambda_e^2 k^2)$$

where λ_e is the electron inertial length, λ_p is the proton inertial length, and β_e is the ratio between the electron plasma thermal pressure and the magnetic pressure. Although the distinct discrepancy between fluid and kinetic models arises at harmonics of ω_{cp}, which results from the high-order cyclotron wave–particle interactions between ions and waves (Sun et al. 2021), v_p predicted by the fluid model is approximately consistent with that given by the kinetic model for the majority of the highly oblique fast-magnetosonic whistler wave. We note that the harmonic waves above ω_{cp} from the kinetic theory are also all identified as ion Bernstein waves (e.g., Podesta 2012); due to the similarity between the harmonic waves with large group speeds ($\gtrsim V_A$) and the oblique fast-magnetosonic whistler wave predicted from the fluid model, we prefer to consider these harmonic waves as consisting of two mode parts, the fast-magnetosonic whistler part and the ion Bernstein part, following the suggestion by López et al. (2017).

Basing on these theoretical predictions of v_p and considering different data set labeled in Figures 5(b) and (c), we can conjecture ω_{pl} and k for each candidate.

1. v_p of the oblique slow mode wave depends on the wave-normal angle, i.e., $v_p = C_S\cos(\theta)$. When the data set is limited to $\theta_{BV} < 10°$ (Figure 5(c)), which indicates that the solar wind nearly streams along the magnetic field, V_k is about $V\cos(\theta)$. Therefore, if the observed waves are oblique slow mode waves, we can estimate the wavenumber through the relation $k_\parallel \sim \omega_{sc}/(C_S + V)$, and the result is $\lambda_p k_\parallel \sim 2$–$39$, which corresponds to $\omega_{pl} = \sqrt{3\beta_p + \beta_e}\,\lambda_p k_\parallel \omega_{cp} \sim 2-39\omega_{cp}$. However, due to significant damping of oblique slow mode waves, their frequencies seem unable to exceed the proton cyclotron frequency (see Figures 5(d) and (e); also see Narita & Marsch 2015).
2. For ion Bernstein waves, we simply consider their v_p to be about 0.1–$2V_A$. When we consider a particular data set in which $\theta_{BV} = 42.^\circ5$–$47.^\circ5$ (circles in Figure 5(b)), V_k would be located between $(\sqrt{2}/2)V$ and V. We can then estimate the lower boundary of the wavenumber through $k_{lower} \sim \omega_{sc}/(2V_A + V)$ and its upper boundary through $k_{upper} \sim \omega_{sc}/(0.1V_A + \sqrt{2}V/2)$. The results are $\lambda_p k_{lower} \sim 1$–$19$ and $\lambda_p k_{upper} \sim 21$–$428$. Due to harmonic structures of ion Bernstein waves, it is hard to estimate the corresponding wave frequency.
3. v_p of the oblique fast-magnetosonic whistler mode wave is about or even larger than $V_A(1 + \beta_p + \beta_e)^{1/2} \sim 2V_A$. This velocity is always larger than V_k ($V_k < V$) in the sub-Alfvénic solar wind (solid triangles in Figure 5(b)), indicating that $\omega_{sc} \sim \omega_{pl}$ in such a solar wind environment. If the observed waves are oblique fast-magnetosonic whistler waves, we conjecture that $\omega_{pl} \sim 3$–$60\omega_{cp}$ (~ 0.1–$1 \times 2\pi f_{LH}$). The wavenumber corresponding to this frequency range is about $\lambda_p k \sim 1$–30 as $\theta \sim 75°$–$89.^\circ9$. Moreover, when the data set with $\theta_{BV} = 42.^\circ5$–$47.^\circ5$ (circles in Figure 5(b)) is considered, the upper boundary of the wavenumber is estimated via $k_{upper} \sim \omega_{sc}/(2V_A + \sqrt{2}V/2)$, that is, $\lambda_p k_{upper} \sim 1$–$21$, which is nearly consistent with that resulting from the data set in the sub-Alfvénic solar wind.

The aforementioned theoretical predictions are based on a two-component (proton and electron) plasma model that is a preliminary approximation of the actual plasma environment in the near-Sun solar wind (see Klein et al. 2021), and hence our conjectures merely provide qualitative clues for the possible wave mode. We note that Vasko et al. (2022) recently proposed the existence of oblique ion acoustic waves with frequencies of several tenths of f_{ce} around the ramp of the quasi-perpendicular Earth's bow shock, where the actual plasma highly deviates from the ideal two-component plasma. We also note that in high-beta plasma environments, near-perpendicular fast-magnetosonic whistler and ion Bernstein waves could have a weak damping rate.

5. Summary and Discussion

This Letter provides the first observational evidence for the existence of broadband electrostatic waves below f_{ce} in the near-Sun solar wind and in the extended solar corona. The observed frequencies are mainly in the range 0.3–$2f_{LH}$, and the frequency bands are mainly in the range 1–$6f_{LH}$. The wave amplitudes are about 0.1–50 mV m^{-1}. This Letter also demonstrates the existence of electrostatic solitary structures where the electric field can reach 500 mV m^{-1}.

Broadband quasi-electrostatic waves with a similar frequency feature (i.e., near f_{LH}) were found in the Earth's space environment (e.g., the magnetopause; see Graham et al. 2019), where these waves are identified as lower-hybrid waves. However, due to the lack of high-resolution particle and three-dimensional electromagnetic field measurements from PSP, we cannot provide a direct observational identification for the mode nature of the observed waves. This Letter proposes several conjectures for the mode nature. Owing to the considerable perpendicular electric fields, we propose that the observed waves cannot be parallel ion acoustic waves that only have parallel electric fields. Because the quasi-electrostatic wave modes below f_{ce} include the oblique slow mode wave, the ion Bernstein wave, and the oblique fast-magnetosonic whistler wave, we describe the wave information for each candidate in this Letter. We note that there is an inconsistency between theoretical predictions and observational results. No matter which oblique wave mode is responsible for the observed waves, the wave theory predicts the existence of the magnetic field perturbations. However, PSP does not detect evident signatures of the magnetic field perturbations. A possible reason is that magnetic signatures are below the SCM noise floor (Bowen et al. 2020), which will be studied in the future.

For the excitation mechanism of the observed waves, previous studies have explored that different types of (quasi-) electrostatic mode waves can be driven by the plasma instabilities (e.g., Forslund 1970; Kindel 1971; Marsch & Chang 1982, 1983; Sun et al. 2021; Verscharen et al. 2022). Forslund (1970) and Kindel (1971) have shown that the ion

acoustic wave and the ion Bernstein wave (or the electrostatic ion cyclotron wave) can be driven by the current instabilities. Marsch & Chang (1982, 1983) and Sun et al. (2021) have shown that the lower-hybrid wave can be produced by the electron flux instability in the solar wind. It should be noted that the two instability mechanisms, i.e., the ion Bernstein wave driven by the current and the lower-hybrid wave driven by the electron flux, are significantly dependent on the plasma beta, and they easily arise in the low-beta plasma environment (Sun et al. 2021; Verscharen et al. 2022) but not in the high-beta plasma environment. In addition, lower-hybrid waves would be excited through the modified two-stream instability in the presence of perpendicular streaming particles (e.g., McBride et al. 1972; Wu et al. 1983; Graham et al. 2019) and through the lower-hybrid drift instability in the presence of a density and/or magnetic gradient (e.g., Krall & Liewer 1971; Davidson et al. 1977; Graham et al. 2019). Among these theoretical instability studies, it appears that the instabilities relating to lower-hybrid waves could produce waves with a similar scale to that suggested in Section 4 (Graham et al. 2019; Sun et al. 2021). For example, Sun et al. (2021) predicted the excitation of lower-hybrid waves with $\lambda_e k \simeq 0.2$ and $f_{\rm pl}/f_{\rm LH} \simeq 0.2$. However, these instability analyses are performed using plasma parameters that are not consistent with the actual plasma environment shown in this Letter. Due to the same limitation of the current instability (Forslund 1970; Kindel 1971), we are unable to preclude the possible connections of the slow mode wave and ion Bernstein wave with the observed waves. We plan to study the instability by using the plasma parameters from PSP in the future, which will provide more theoretical clues for identifying the wave modes.

Because the observed waves carry considerably large electric fields, they can play significant roles in the particle energization in the near-Sun solar wind and in the solar corona. Through parallel electric fields, these waves can interact with particles through Landau wave–particle interactions. The perpendicular electric field can result in cyclotron interactions with particles. Thus, we expect particle energization by these waves.

Lastly, the observed broadband electrostatic waves may be closely related to the mechanism regulating the electron heat flux in the near-Sun solar wind (Sun et al. 2021). Recently, the regulation of electron heat flux therein seems unable to be induced by two popular mechanisms relating to the parallel and oblique whistler waves (Cattell et al. 2022; Jeong et al. 2022). Cattell et al. (2022) found the absence of whistler waves in the solar wind close to the Sun by using PSP observations; Jeong et al. (2022) showed that the oblique whistler heat flux instability cannot be triggered by the electron strahl in the inner heliosphere from Helios and PSP observations. Because the observed broadband electrostatic waves are often found in the near-Sun solar wind, they could result in scattering of the strahl electrons in the near-Sun solar wind. These speculations based on the data will be investigated further in future work.

This work was supported by the National Key R&D Program of China 2021YFA1600502 (2021YFA1600500) and the NSFC 41974203. S.P. acknowledges financial support via the projects C14/19/089 (C1 project Internal Funds KU Leuven), G.0D07.19N (FWO-Vlaanderen), SIDC Data Exploitation (ESA Prodex-12), and Belspo project B2/191/P1/SWiM. Parker Solar Probe was designed, built, and is now operated by the Johns Hopkins Applied Physics Laboratory as part of NASA's Living with a Star (LWS) program (contract NNN06AA01C). All data used in this paper are publicly available from the links http://fields.ssl.berkeley.edu/data/ and http://sweap.cfa.harvard.edu/pub/data/sci/sweap/. We appreciate the referee for inspiring comments and helpful suggestions.

ORCID iDs

Jinsong Zhao https://orcid.org/0000-0002-3859-6394
David M. Malaspina https://orcid.org/0000-0003-1191-1558
T. Dudok de Wit https://orcid.org/0000-0002-4401-0943
Viviane Pierrard https://orcid.org/0000-0001-5014-7682
Yuriy Voitenko https://orcid.org/0000-0002-4139-1795
Giovanni Lapenta https://orcid.org/0000-0002-3123-4024
Stefaan Poedts https://orcid.org/0000-0002-1743-0651
Stuart D. Bale https://orcid.org/0000-0002-1989-3596
Justin C. Kasper https://orcid.org/0000-0002-7077-930X
Davin Larson https://orcid.org/0000-0001-5030-6030
Roberto Livi https://orcid.org/0000-0002-0396-0547
Phyllis Whittlesey https://orcid.org/0000-0002-7287-5098

References

Agapitov, O. V., Dudok de Wit, T., Mozer, F. S., et al. 2020, ApJL, 891, L20
Bale, S. D., Goetz, K., Harvey, P. R., et al. 2016, SSRv, 204, 49
Bowen, T. A., Bale, S. D., Bonnell, J. W., et al. 2020, JGRA, 125, e27813
Bowen, T. A., Mallet, A., Huang, J., et al. 2020, ApJS, 246, 66
Cattell, C., Breneman, A., Dombeck, J., et al. 2021, ApJL, 911, L29
Cattell, C., Breneman, A., Dombeck, J., et al. 2022, ApJL, 924, L33
Davidson, R. C., Gladd, N. T., Wu, C. S., & Huba, J. D. 1977, PhFl, 20, 301
Dudok de Wit, T., Krasnoselskikh, V. V., Agapitov, O., et al. 2022, JGRA, 127, e30018
Forslund, D. W. 1970, JGR, 75, 17
Graham, D. B., Khotyaintsev, Y., Norgren, C., et al. 2019, JGRA, 124, 8727
Graham, D. B., Khotyaintsev, Y. V., Vaivads, A., et al. 2021, A&A, 656, A23
Halekas, J. S., Whittlesey, P., Larson, D. E., et al. 2020, ApJS, 246, 22
Jagarlamudi, V. K., Dudok de Wit, T., Froment, C., et al. 2021, A&A, 650, A9
Jeong, S. Y., Abraham, J. B., Verscharen, D., et al. 2022, ApJL, 926, L26
Kasper, J. C., Abiad, R., Austin, G., et al. 2016, SSRv, 204, 131
Kasper, J. C., Klein, K. G., Lichko, E., et al. 2021, PhRvL, 127, 255101
Kindel, J. M., & Kennel, C. F. 1971, JGR, 76, 3055
Klein, K. G., Verniero, J. L., Alterman, B., et al. 2021, ApJ, 909, 7
Krall, N. A., & Liewer, P. C. 1971, PhRvA, 4, 2094
Livi, R., Davin, E. L., Kasper, J. C., et al. 2021, Earth and Space Science Open Archive, doi:10.1002/essoar.10508651.1
López, R. A., Viñas, A. F., Araneda, J. A., et al. 2017, ApJ, 845, 60
Malaspina, D. M., Ergun, R. E., Bolton, M., et al. 2016, JGRA, 121, 5088
Malaspina, D. M., Halekas, J., Berčič, L., et al. 2020, ApJS, 246, 21
Malaspina, D. M., Newman, D. L., Willson, L. B., et al. 2013, JGRA, 118, 591
Malaspina, D. M., Wilson, L. B., Ergun, R. E., et al. 2021, A&A, 650, A97
Marsch, E., & Chang, T. 1982, GeoRL, 9, 1155
Marsch, E., & Chang, T. 1983, JGR, 88, 6869
McBride, J. B., Ott, E., Boris, J. P., et al. 1972, PhFl, 15, 2367
Mozer, F. S., Agapitov, O. V., Bale, S. D., et al. 2020a, JGRA, 125, e27980
Mozer, F. S., Bonnell, J. W., Bowen, T. A., et al. 2020b, ApJ, 901, 107
Mozer, F. S., Bonnell, J. W., Hanson, E. L. M., et al. 2021a, ApJ, 911, 89
Mozer, F. S., Vasko, I. Y., & Verniero, J. L. 2021b, ApJL, 919, L2
Narita, Y., & Marsch, E. 2015, ApJ, 805, 24
Podesta, J. J. 2012, JGRA, 117, A07101
Pulupa, M., Bale, S. D., Badman, S. T., et al. 2020, ApJS, 246, 49
Reid, H. A. S., & Ratcliffe, H. 2014, RAA, 14, 773
Shi, C., Zhao, J., Huang, J., et al. 2021, ApJL, 908, L19
Shi, C., Zhao, J., Malaspina, D. M., et al. 2022, ApJL, 926, L3
Sun, H., Zhao, J., Liu, W., et al. 2021, ApJL, 916, L4
Vasko, I. Y., Mozer, F. S., Bale, S. D., et al. 2022, GeoRL, 49, e98640
Verniero, J. L., Larson, D. E., Livi, R., et al. 2020, ApJS, 248, 5
Verscharen, D., Chandran, B. D. G., Boella, E., et al. 2022, FrASS, 9, 951628
Verscharen, D., Chen, C. H. K., & Wicks, R. T. 2017, ApJ, 840, 106
Verscharen, D., Klein, K. G., & Maruca, B. A. 2019, LRSP, 16, 5
Whittlesey, P. L., Larson, D. E., Kasper, J. C., et al. 2020, ApJS, 246, 74
Wu, C. S., Winske, D., Papadopoulos, K., et al. 1983, PhFl, 26, 1259
Zhao, J. 2015, PhPl, 22, 042115
Zhao, J. S., Voitenko, Y., Yu, M. Y., et al. 2014, ApJ, 793, 107